catalysts

MDPI

Article

An Effective Strategy to Enhance the Electrocatalytic Activity of Ruddlesden−Popper Oxides $Sr_3Fe_2O_{7-\delta}$ Electrodes for Solid Oxide Fuel Cells

Longsheng Peng, Qiang Li *, Liping Sun and Hui Zhao *

Key Laboratory of Functional Inorganic Material Chemistry, Ministry of Education, School of Chemistry and Materials Science, Heilongjiang University, Harbin 150080, China; P021001@hlju.edu.cn (L.P.); sunliping@hlju.edu.cn (L.S.)

* Correspondence: liqiang@hlju.edu.cn (Q.L.); zhaohui@hlju.edu.cn (H.Z.)

Abstract: The target of this work is to develop advanced electrode materials with excellent performance compared to conventional cathodes. Cobalt-free Ruddlesden−Popper oxides $Sr_3Fe_{2-x}Cu_xO_{7-\delta}$ (SFCx, x = 0, 0.1, 0.2) were successfully synthesized and assessed as cathode materials for solid oxide fuel cells (SOFCs). Herein, a Cu-doping strategy is shown to increase the electrical conductivity and improve the electrochemical performance of the pristine $Sr_3Fe_2O_{7-\delta}$. Among all the cathode materials, the $Sr_3Fe_{1.9}Cu_{0.1}O_{7-\delta}$ (SFC10) cathode exhibits the best electrocatalytic activity for oxygen reduction reaction (ORR). The polarization resistance is 0.11 Ω cm^2 and the peak power density of the single-cell with an SFC10 cathode reaches 955 mW cm^{-2} at 700 °C, a measurement comparable to cobalt-based electrodes. The excellent performance is owed to favorable oxygen surface exchange capabilities and larger oxygen vacancy concentrations at elevated temperatures. Moreover, the electrochemical impedance spectra and distribution of relaxation time results indicate that the charge transfer process at the triple-phase boundary is the rate-limiting step for ORR on the electrode. This work provides an effective strategy for designing novel cathode electrocatalysts for SOFCs.

Keywords: solid oxide fuel cells; cathode material; Ruddlesden−Popper oxides; electrochemical performance

Citation: Peng, L.; Li, Q.; Sun, L.; Zhao, H. An Effective Strategy to Enhance the Electrocatalytic Activity of Ruddlesden−Popper Oxides $Sr_3Fe_2O_{7-\delta}$ Electrodes for Solid Oxide Fuel Cells. *Catalysts* **2021**, *11*, 1400. https://doi.org/10.3390/catal11111400

Academic Editor: Nicolas Alonso-Vante

Received: 21 October 2021
Accepted: 16 November 2021
Published: 18 November 2021

1. Introduction

Mixed ionic and electronic conductor (MIEC) materials are generally considered to be promising cathode candidates for solid oxide fuel cells (SOFCs) [1,2]. Among several MIEC oxides, Ruddlesden−Popper (R–P) materials have aroused attention due to their high electronic conductivity and favorable stability [3,4]. The R–P oxidizes with the general structural formula of $A_{n+1}B_nO_{3n+1}$ (A = alkaline earth and/or rare earth elements, B = transition metal), where perovskite slabs are sandwiched between rock-salt layers [5,6]. Among the R–P oxides, our interest was mainly focused on n = 1 oxides as oxygen electrodes, in which one BO_6 octahedron layer alternately distributes with a single AO rock-salt layer along the c axis, such as La_2NiO_4, Pr_2NiO_4 and Pr_2CuO_4 [7–9]. However, their electrochemical performance for ORR is dissatisfactory at intermediate temperatures [10,11].

Recently, the R–P structure (n = 2) oxide $Sr_3Fe_2O_{7-\delta}$ has gained attention because of its larger oxygen capacity and outstanding stability at high temperatures [12]. The oxide $Sr_3Fe_2O_{7-\delta}$ consists of two $SrFeO_3$ perovskite layers and a rock-salt SrO layer structure alternately stacked. [13,14]. Recent studies showed that the Co-doping in Fe-site could enhance the oxygen vacancy concentration and the electrochemical performance of the $Sr_3Fe_2O_{7-\delta}$ cathode [15,16]. Nevertheless, these Co-containing cathodes show some disadvantages, such as poor thermochemical durability, high thermal expansion coefficient and cobalt evaporation, leading to performance degradation during long-term work [17,18]. For this purpose, the electrode performance of cobalt-free based-$Sr_3Fe_2O_{7-\delta}$ cathodes is worth investigating for SOFCs.

In this work, we prepared cobalt-free R–P type oxides, $Sr_3Fe_{2-x}Cu_xO_{7-\delta}$ (SFCx, x = 0, 0.1, 0.2), and evaluated the potential application of SFCx as an electrode for SOFCs. The ORR kinetics and electrochemical activity of SFCx cathodes were intensively investigated. The ORR kinetic processes on the cathode were comprehensively analyzed by the electrochemical impedance spectra.

2. Results

The XRD spectra of the SFCx samples are shown in Figure 1a. All diffraction patterns of the samples were assigned to $Sr_3Fe_2O_7$ (JCPDS no. 45-0398) with a tetragonal I4/mmm structure. The magnified patterns at 2θ = 31−35° show that the diffraction peak has a shift to a higher angle with the substitution amount of Cu (Figure 1b), demonstrating the contraction of lattice cells. To understand the detailed lattice parameters of the SFCx oxides, Rietveld refinements are presented in Figure 1c,d and fitted structural parameters are shown in Table S1. The satisfactory χ^2, R_{wp} and R_p values prove reliable slotting between the calculated result and the observed patterns. Moreover, the cell volume systematically decreases from 300.892 Å^3 (SFO) to 299.031 Å^3 (SFC20) with Cu-doping content increasing, which can be attributed to the smaller Cu^{2+} (0.73 Å) radius partially substituting Fe^{3+} (0.79 Å) cation. The chemical compatibility between the electrode and the electrolyte is an important factor affecting the electrochemical activity of the cathode. Therefore, the SFCx and GDC powders were mixed and then calcined at 1000 °C for 12 h. The corresponding XRD spectra of the mixture are presented in Figure 1f. All diffraction peaks in the pattern can be assigned to either SFCx or GDC and no undesired phases can be observed. These results reveal that SFCx cathodes and GDC electrolytes possess favorable chemical compatibility at high temperatures.

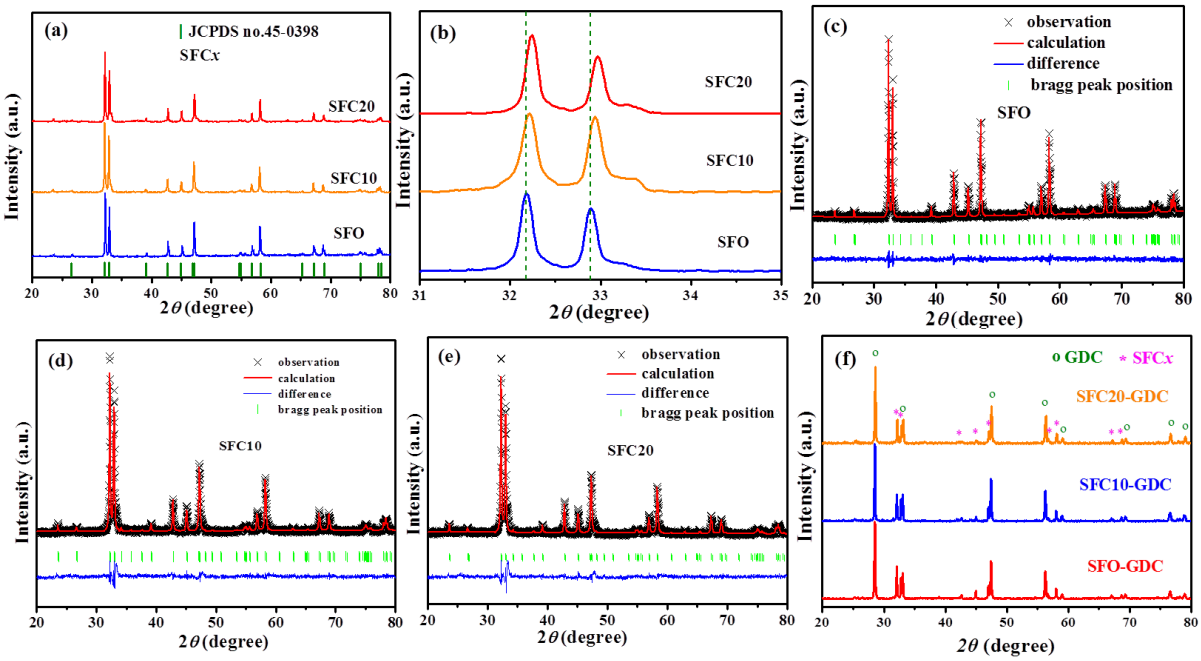

Figure 1. (**a**) XRD spectra of SFCx samples; (**b**) XRD pattern of SFCx within a diffraction angle of 2θ = 31–35°; the refined XRD patterns of SFO (**c**), SFC10 (**d**) and SFC20 (**e**); (**f**) XRD spectra of SFCx-GDC composite after being calcined at 1000 °C for 12 h.

Figure 2a shows the HR-TEM of the SFC10 sample. The crystallized lattice fringes with distances of 0.181 nm and 0.254 nm agree well with the (200) and (110) planes in the SFC10 phase, respectively (Figure 2b), as revealed in the respective intensity distribution figures of the lattice planes (Figure 2c). This result is demonstrated by the fast Fourier transform (FFT) pattern along the [010] zone axis, with the correlative (200) and (110) diffraction planes, as displayed in Figure 2d.

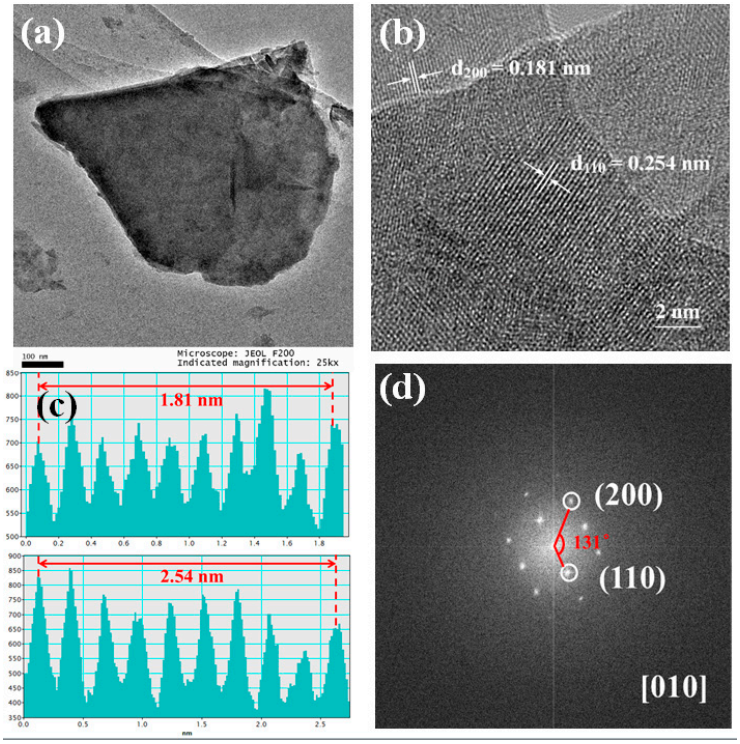

Figure 2. (**a**) HR-TEM figure of the SFC10 sample; (**b**) lattice fringes of the magnified HR-TEM image; (**c**) intensity distribution figures of crystalline fringes matching to (**b**); (**d**) FFT pattern of the SFC10 sample.

Figure 3a shows the XPS response of O 1s of the SFC*x* materials. It is evident that the lower binding energy at 530.6–531 eV is attributable to lattice oxygen (O_{lat}) [19], and the higher binding energy peaks at 531.5–532.3 eV are related to adsorbed oxygen (O_{ads}) consisting of OH^-, O^{2-}, O^- and carbonate [20]. According to the fitting peaks, the peak area ratios of O_{ads}/O_{lat} are 5.41, 14.97 and 7.46 for SFO, SFC10 and SFC20, respectively (Table 1). It is noteworthy that the SFC10 material shows the highest ratio of O_{ads}/O_{lat}, indicating the excellent oxygen adsorption ability of SFC10 oxide [21]. In addition, Figure 3b shows the Fe $2p_{3/2}$ spectra of SFC*x* samples. The spectra can be deconvoluted into three peaks, which correspond to Fe^{2+} (709.1–709.8 eV), Fe^{3+} (710.1–712.2 eV) and Fe^{4+} (712.4–713.5 eV), respectively [22,23]. The percentages of the different valence states and the average oxidation state of iron in SFC*x* samples are listed in Table 1. We found that the proportion of Fe^{4+} and Fe^{3+} cations decreases and Fe^{2+} content increases after Cu doping, indicating that reduction of Fe ions from Fe^{4+}/Fe^{3+} to Fe^{3+}/Fe^{2+} occurs in the SFC*x* materials. Moreover, the calculated oxygen non-stoichiometry (δ, oxygen vacancy concentration) of SFC*x* is 0.906, 1.09 and 1.211 for SFO, SFC10 and SFC20, respectively, suggesting that Cu-doping improves oxygen vacancy concentration.

O_2-TPD is an effective method for evaluating the oxygen exchange capability of the oxide. Figure 4a displays the O_2-TPD plots of SFC*x* samples. Two obvious desorption peaks are observed in the samples. The first desorption peak at 250–550 °C corresponds to the α-oxygen desorption, resulting from the reduction of Fe^{4+} to Fe^{3+} and chemisorbed oxygen desorption on the surface [24]. The second peak, at around 800 °C, can be attributed to β-oxygen desorption with the further reduction of Fe^{3+} to Fe^{2+} [25]. It is observable that the peak areas of α-oxygen desorption for SFC10 and SFC20 are higher than those of SFO, confirming that Cu doping improves the oxygen surface exchange capability. It should be noted that the SFC10 sample presents the highest peak area of α-oxygen desorption among the SFC*x* materials, suggesting a higher oxygen vacancy concentration and better oxygen ionic mobility of the compound. The oxygen non-stoichiometry (δ) of the SFC*x* materials at elevated temperatures was investigated by the TGA. The δvalues are calculated

by combining the TGA result and the oxygen non-stoichiometric values (δ_0) of SFCx at room temperature as obtained by the iodometric titration method. We found that the weight of SFCx materials stays unchanged from 50 to 250 °C. When the temperature is over 250 °C, the rapid weight loss can be attributed to the release of the lattice oxide, which corresponds to the reduction of Fe ions and then the generation of oxygen vacancy [26], as shown in Figure 4b. The formation of the oxygen vacancy can be written in Kröger–Vink (KV) notation (1) as follows:

$$2Fe_{Fe}^{\bullet}+O_O^{\times} \triangleq 2Fe_{Fe}^{\times}+V_O^{\bullet\bullet}+\frac{1}{2}O_2\uparrow, \quad (1)$$

In addition, it is a remarkable fact that the SFC10 material shows the highest δ values at a temperature range of 50–900 °C, which indicates more oxygen vacancies. Generally, a higher oxygen vacancy concentration can improve the oxygen ion migration capability in the electrode material, thus enhancing the electrocatalytic activity toward ORR of the cathode electrocatalyst [27,28].

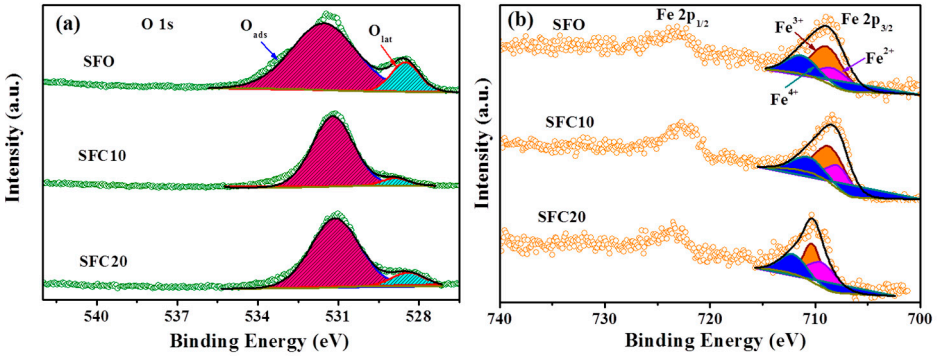

Figure 3. (**a**) O 1s and (**b**) Fe $2p_{3/2}$ spectra of SFCx samples.

Table 1. Percentages of different iron and oxygen, ratios of O_{ads}/O_{lat}, average oxidation states of iron and the oxygen non-stoichiometry.

	Fe $2p_{3/2}$ (%)			O 1s (%)			Average Valence Fe	δ
Sample	**Fe^{4+}**	**Fe^{3+}**	**Fe^{2+}**	**O_{ads}**	**O_{lat}**	**O_{ads}/O_{lat}**		
SFO	26.85	55.71	17.45	84.39	15.61	5.41	3.094	0.906
SFC10	21.60	52.60	25.80	93.74	6.26	14.97	2.958	1.090
SFC20	18.84	50.04	31.12	88.19	11.81	7.46	2.877	1.211

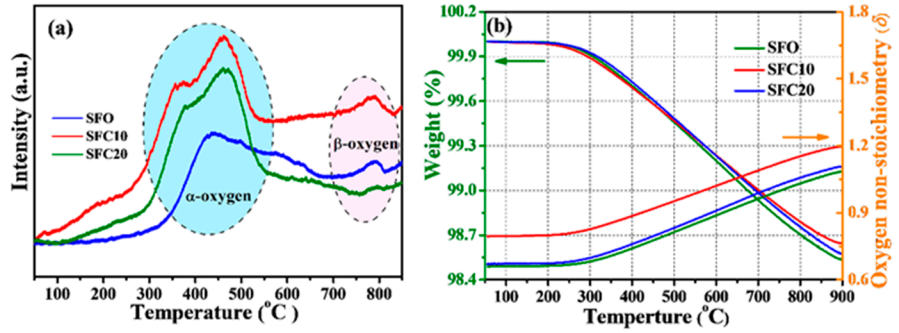

Figure 4. (**a**) O_2-TPD profiles of SFCx oxides; (**b**) thermogravimetry and oxygen non-stoichiometry of the SFCx samples.

Figure 5a exhibits the relationship between the electrical conductivity of the SFCx samples and temperature. The electrical conductivity of the SFCx samples initially increases with temperature to reach a maximum value at 450 °C, revealing the semi-conducting mechanism. At temperatures above 450 °C, the electrical conductivity decreases along with

the temperature, indicating its dominant metallic-conducting behavior. This phenomenon arises due to the thermal-induced reduction of the Fe/Cu ions and the release of lattice oxygen [29]. The maximum values of electrical conductivity are 57, 196 and 75 S cm^{-1} for SFO, SFC10 and SFC20, respectively. It is noteworthy that the maximum value of the SFC10 at 100–800 °C is remarkably superior to some Fe series materials for SOFCs, as shown in Figure 5b [30–37].

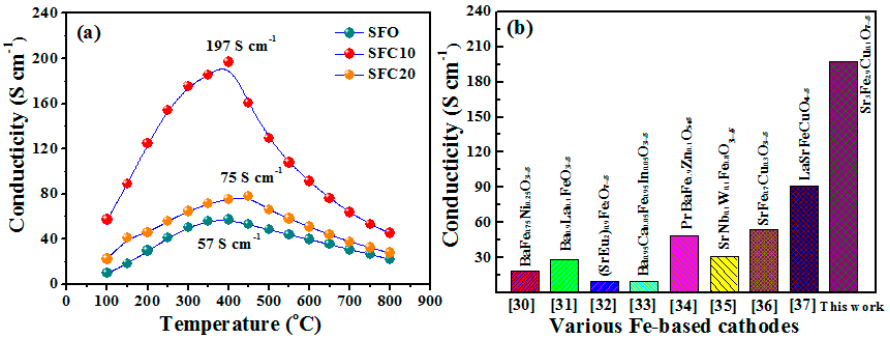

Figure 5. (**a**) Electrical conductivity of the SFC*x* materials at 100,800 °C; (**b**) maximum value of the conductivity for various Fe-based cathodes.

The electrocatalytic performance for ORR of the cathodes is determined by symmetrical cell (SFC*x* | GDC | SFC*x*). Figure 6a exhibits Nyquist plots of the SFC*x* cathodes at 700 °C under open-circuit voltage. The impedance spectra consist of two distinguishable high-frequency (HF) and low-frequency (LF) zones, inferring that the two electrode processes occur on the electrode. Furthermore, the impedance data are fitted by an equivalent circuit model of $R_{ohm} - (R_{HF} - CPE_{HF}) - (R_{LF} - CPE_{LF})$ (inset in Figure 6a), where R_{ohm} represents the overall ohmic resistance, including the electrolyte and wire resistance; R_{HF} and R_{LF} represent the polarization resistance of the HF region and the LF region; CPE_{HF} and CPE_{LF} are the constant phase elements. The SFC*x* cathodes present favorable electrochemical activity, as displayed in Figure 6a. The R_p values of SFO, SFC10 and SFC20 cathode materials are 0.39, 0.11 and 0.18 Ω cm^2 at 700 °C, respectively. Noticeably, the SFC10 cathode exhibits the lowest R_p value among the SFC*x* cathodes at 700 °C, which is much smaller than the reported R–P type cathodes [38–43] (Figure 6b), suggesting the great promise of SFC10 as a high electrochemical activity cathode electrocatalyst. Additionally, the activation energy (E_a) of the cathodes was obtained from the Arrhenius plot, as presented in Figure 6c. The calculated E_a values are 129.60, 138.24 and 142.08 kJ mol^{-1} for SFC10 and SFC20, respectively. These values are lower than some Fe series electrodes, such as $Ba_{0.9}Nb_{0.1}FeO_{3-\delta}$ (153.33 kJ mol^{-1}) [44], $LaFe_{0.8}Cu_{0.2}O_{3-\delta}$ (159.2 kJ mol^{-1}) [45] $La_{0.6}Sr_{0.4}Co_{0.2}Fe_{0.8}O_{3-\delta}$ (166 kJ mol^{-1}) [46] and $La_{0.5}Sr_{0.5}Fe_{0.9}Mo_{0.1}O_{3-\delta}$ (178 kJ mol^{-1}) [47]. Additionally, to understand the electrochemical process of the overall reaction, electrochemical impedance spectroscopy (EIS) is further analyzed by the distribution of the relaxation times (DRT) method. The DRT plots of the SFC*x* cathodes at 700 °C are depicted in Figure 6d. Each plot shows two distinct peaks: LF peak (P_{LF}) and HF peak (P_{HF}). This suggests two electrode processes are occurring on the SFC10 cathode [48]. It is also worth noting that the peak areas of P_{LF} for the SFC10 and SFC20 cathodes are significantly lower than those of the SFO, whereas the peak areas of P_{HF} demonstrate a slight change, which means that Cu doping mainly affects electrode reaction at low-frequency zone.

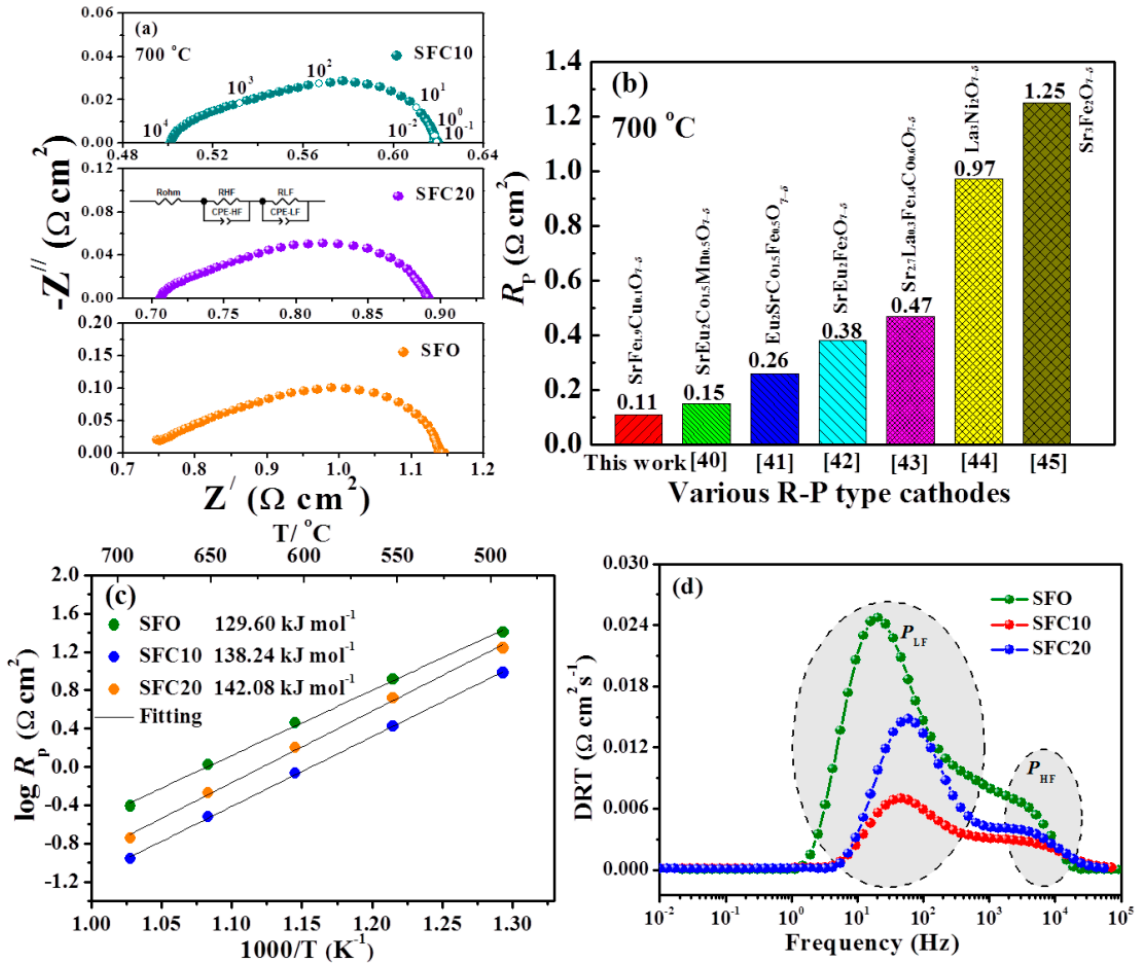

Figure 6. (**a**) EIS patterns of SFC*x* cathode collected at 700 °C in air; (**b**) R_p value of various Ruddlesden−Popper-type cathode materials at 700 °C; (**c**) Arrhenius curves of polarization resistance for SFC*x* cathode materials at 500–700 °C; (**d**) DRT analysis of the impedance spectra for SFC*x* electrodes at 700 °C.

The electrochemical reaction mechanism of SFC*x* cathode, the characteristic capacitance (C) and the relaxation frequency (f) are attained according to the following Equations [49]:

$$C_k = \frac{(R_k Q_k)^{(1/n_k)}}{R_k}, \quad (2)$$

$$f_k = \frac{(R_k Q_k)^{-(1/n_k)}}{2\pi}, \quad (3)$$

The C and f values of SFC*x* cathodes at 700 °C are listed in Table 2. For the high-frequency region, C_H and f_H are 10^{-5}–10^{-4} F cm^{-2} and 10^3 Hz, respectively, which might be associated with the oxygen ion transfer process [50]. For the low-frequency region, C_L and f_L are 10^{-3}–10^{-2} F cm^{-2} and 10^1–10^2 Hz, respectively, where the LF response is associated with the oxygen adsorption–dissociation process [51].

To further explain the ORR mechanism of the cathode, the EIS spectra of the SFC10 electrode were systematically evaluated under various oxygen partial pressures (Po_2) at 700 °C, as shown in Figure 7a. As shown, the impedance spectra consist of two semi-circular arcs, suggesting that the two different processes for ORR existed on the cathode. The electrochemical processes of the electrode have different relationships with the oxygen partial pressure [52]. The relationship between R_p and Po_2 is represented accordingly: $R_p = R_0(Po_2)^{-m}$ (4), where m is the detailed electrochemical reaction step for ORR. Figure 7b illustrates the relationship between Po_2 and the HF (R_H) and LF (R_L)

resistances of the SFC10 electrode at 700 °C. The attained m values for R_H and R_L are 0.073 and 0.385, respectively. These results prove that the HF process is related to the oxygen ions' transfer at the electrode/electrolyte (m = 0, $O^{2-}_{TPB}+V^{\bullet\bullet}_{O} \leftrightarrow O^{\times}_{O}$) [53], while the LF process is connected with the charge transfer reaction at the triple-phase boundary (TPB) (m = 3/8, $O_{TPB} + 2e' \leftrightarrow O^{2-}_{TPB}$) [54]. The schematic diagram of the reaction mechanism is shown in Figure 6b. Furthermore, the impedance spectra of the SFL10 cathode are analyzed using the DRT under different Po_2, as plotted in Figure 7c. Evidently, the peak area of the P_{LF} decreases with different Po_2 levels, whereas the peak area of the P_{HF} exhibits no obvious change. It is remarkable that the peak areas of the P_{LF} are larger than those of the P_{HF} under different Po_2, indicating that the charge transfer reaction at TPB is the rate control step on the electrode, which is consistent with the Bode plots under different Po_2 (Figure S1).

Table 2. Equivalent circuit fitting results of the impedance spectra for the SFCx electrodes at 700 °C.

Cathode		SFO	SFC10	SFC20
HF arc	R_{HF} (Ω cm^2)	0.2033	0.0557	0.0689
	CPE_{HF}-Q (F cm^{-2})	0.0091	0.0152	0.00909
	CPE_{HF}-n	0.5150	0.6085	0.6263
	C_{HF} (F cm^{-2})	2.43×10^{-5}	1.60×10^{-4}	1.10×10^{-4}
	f_{HF} (Hz)	3.22×10^{3}	1.78×10^{3}	2.10×10^{3}
LF arc	R_{LF} (Ω cm^2)	0.2055	0.0633	0.1185
	CPE_{LF}-Q (F cm^{-2})	0.0531	0.1040	0.0339
	CPE_{LF}-n	0.8213	0.8161	0.8156
	C_{LF} (F cm^{-2})	1.99×10^{-2}	3.35×10^{-2}	9.73×10^{-3}
	f_{LF} (Hz)	38.963	74.995	138.153

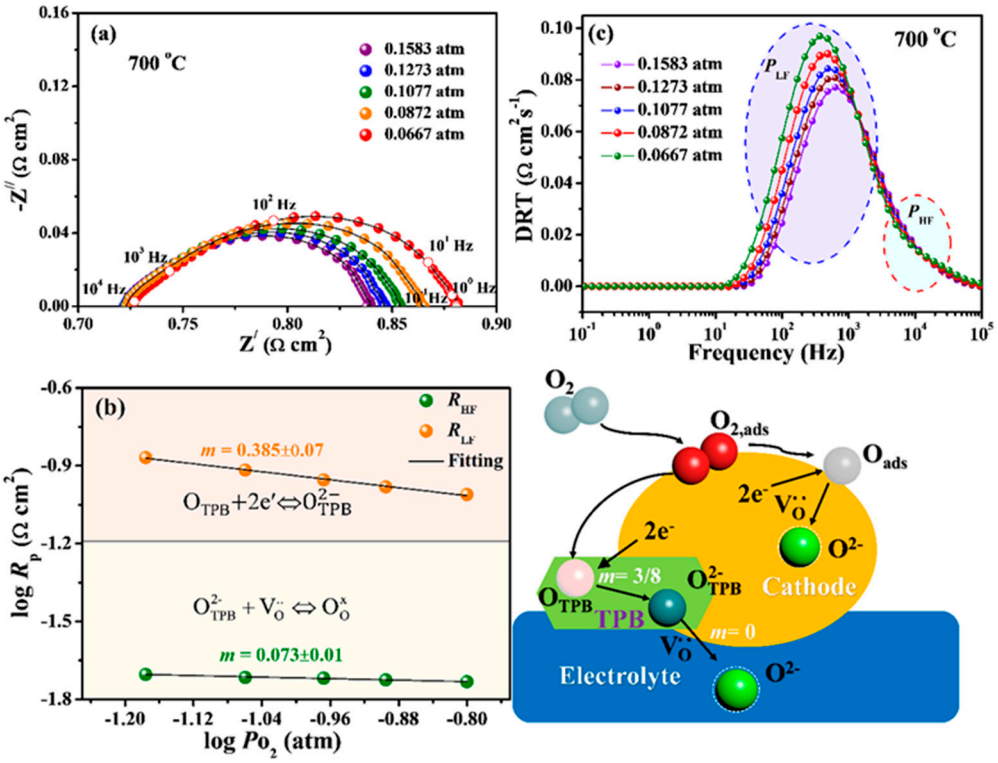

Figure 7. (**a**) Impedance spectra of the SFC10 electrode under various Po_2 at 700 °C; (**b**) R_{HF} and R_{LF} of the SFC10 electrode vs. Po_2 at 700 °C; (**c**) DRT curves of SFC10 electrode under various Po_2.

To further explore the electrocatalytic performance of the SFCx cathodes, a series of anode-supported button cells were prepared and measured at 600–700 °C, as depicted in

Figure 8a and Figure S3. The single cells comprise a ~300 μm-thick Ni-YSZ anode layer, a ~10 μm-thick dense YSZ electrolyte layer, a ~3 μm-thick GDC diffusion barrier layer and a ~20 μm-thick porous SFC*x* cathode material layer, respectively (Figure S2). The maximum power density (MPD) of the fuel cells with SFO, SFC10 and SFC20 cathodes is 351, 955 and 544 mW cm^{-2} at 700 °C, respectively. The optimal performance of the SFC10 cathode may be due to the satisfactory electrochemical activity for ORR. It is worth noting that the MPD of the SFC10 cathode-based fuel cell at 700 °C is higher than that of R–P perovskite cathode materials, such as $Sr_3Fe_{1.9}Ni_{0.1}O_{7-\delta}$ (218 W cm^{-2}) [55], $Sr_3Fe_{1.3}Co_{0.2}Mo_{0.5}O_{7-\delta}$ (300 mW cm^{-2}) [56] and $Sr_3Fe_{1.8}Co_{0.2}O_{7-\delta}$ (840 mW cm^{-2}) [16]. The long-term durability test result of the button cell with SFC10 cathode is depicted in Figure 8b. More importantly, the PPD of the single-cell maintains a steady value without any distinct change for 60 h at 700 °C, revealing that the SFC10 cathode holds satisfactory electrochemical stability. Furthermore, Figure 8c represents a cross-section image of the button cell after a 60 h durability test. Evidently, the SFC10 cathode layer affords appropriate porosity and coheres well with the GDC barrier layer. No obvious crack or delamination at the anode/electrolyte/cathode/barrier layer interfaces is visible, which favors the gas diffusion between the button cell components. The polarization plots of the three-electrode cell were further measured in the SOFC and SOEC modes at different temperatures (Figure 8d). For the SOFC mode, the density reached −150 mA cm^{-2} when the cathode overpotential was −41.28 mV. For the SOEC mode, when the density was 130 mA cm^{-2}, the anode overpotential was 36.61 mV. The above results reveal that the SFC10 material is a promising bifunctional electrode.

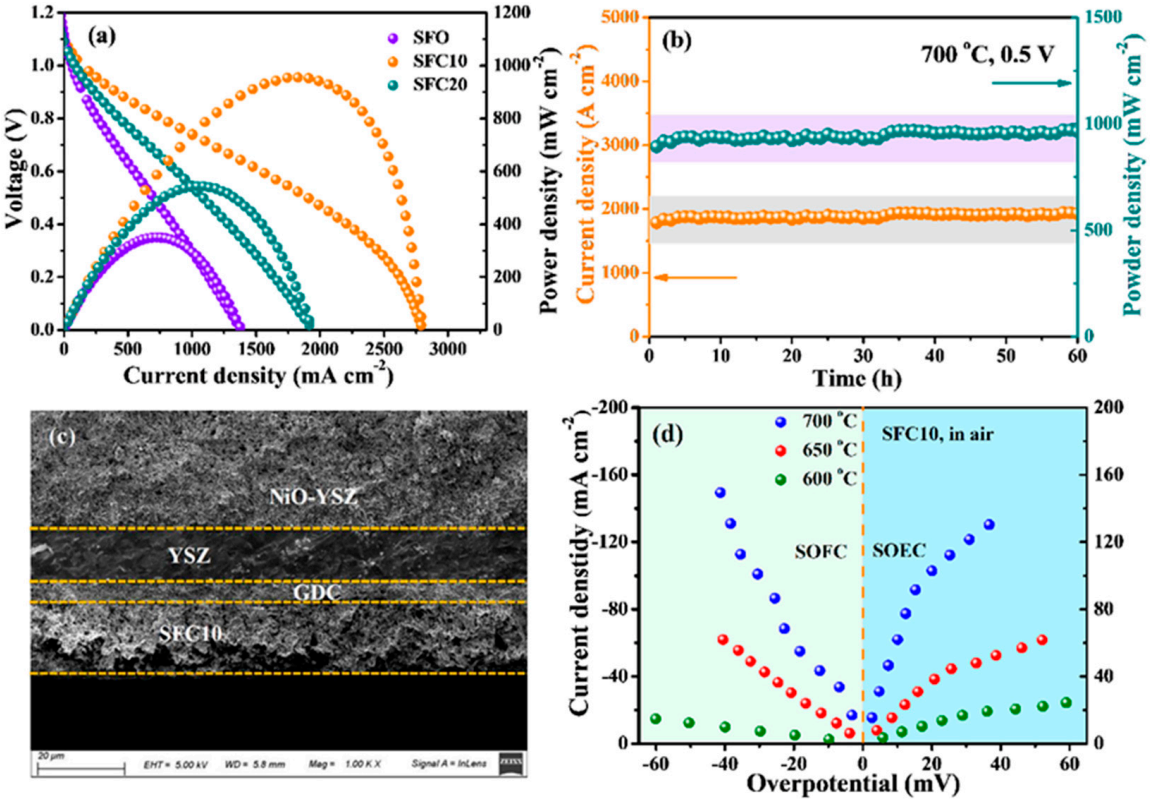

Figure 8. (**a**) *I-V* and *I-P* plots of the button cells NiO/YSZ | YSZ | GDC | SFC*x* at 700 °C; (**b**) short-term durability of SFC10 cathode-based fuel cell at 700 °C; (**c**) cross-sectional SEM image of the fuel cell; (**d**) the polarization plots of SFC10 electrode in SOFC and SOEC modes at various temperatures.

3. Materials and Methods

3.1. Sample Preparation

The $Sr_3Fe_{2-x}Cu_xO_{7-\delta}$ (SFCx, x = 0, 0.1, 0.2) oxides were synthesized by the sol–gel method, denoted as SFO, SFC10 and SFC20, respectively. The stoichiometric amounts of $Sr(NO_3)_2$ (99.5%), $Fe(NO_3)_3{\cdot}9H_2O$ (99.9%) and $Cu(NO_3)_2{\cdot}3H_2O$ (99%) were added into deionized water to form a mixed solution. Subsequently, the ethylenediaminetetraacetic acid (EDTA) and citric acid were dissolved in the above solution, which was used as a precursor solution. The molar ratio of EDTA, citric acid and total metallic ions was 1:2:1. Afterwards, the ammonia was dropped into the solution to adjust the pH to about 7–8, followed by heating until it attained a gel. The resultant gel was heated at 180 °C for 8 h and subsequently sintered at 1100 °C for 12 h to form the desired oxides.

3.2. Fabrication of the Cells

The GDC powder was pressed into discs and calcined at 1400 °C for 12 h to prepare a dense GDC electrolyte. The SFCx powder was mixed with terpineol to obtain a cathode paste. The paste was then applied uniformly to both sides of the GDC disc, followed by sintering at 950 °C for 4 h to form the symmetrical cell. The three-electrode was fabricated according to the reported method in the literature [19]. For the test button cell fabrication, the half-cell NiO/YSZ | YSZ | GDC was purchased from SOFCMAN Energy Co. Ltd (Ningbo, China). The cathode slurries were printed onto the GDC layer and then sintered at 950 °C for 4 h.

3.3. Physico-Chemical Characterization

We analyzed the crystal structures of the oxides with an X-ray diffractometer (Bruker AXSD8 Advance, Bruker AXS GmbH, Karlsruhe, Germany) using Cu Kα radiation. The microstructure was examined by a scanning electron microscope (SEM, Supra 55 Sapphire, Carl ZEISS, Oberkochen, Germany). The detailed crystal structure of the material was obtained by high-resolution transmission electron microscopy (HR-TEM, JEOL-F200, JEOL, Tokyo, Japan). The chemical composition and oxidation state of the elements were analyzed by X-ray photoelectron spectrum (XPS) with a KRATOS spectrometer (Ultra DLD). The oxygen desorption property of SFCx was characterized by the oxygen temperature-programmed desorption (O_2-TPD) method with a dynamic adsorption device (TP-5076). The oxygen non-stoichiometry value (δ) of samples at elevated temperatures was calculated by thermogravimetric analysis (TGA) and iod ometric titration data, as described elsewhere [57]. The electrical conductivity of SFCx materials was conducted via the four-wire method with a Keithley 2700 digital source meter at 100−800 °C.

3.4. Electrochemical Test

The EIS was acquired by the electrochemical workstation (Autolab PROSTAT302 N) in the frequency range of 10^{-2}–10^5 Hz under open-circuit voltage conditions. To clarify the ORR kinetics of the cathode, impedance spectra were collected under different Po_2. The *I-V* and *I-P* plots of the fuel cells were monitored with an electrochemical workstation (IM6ex) at between 600 and 700 °C. We used wet hydrogen and static air as the fuel and oxidation gas, respectively. The polarization plots of the electrode were performed by the three-electrode cell using the chronoamperometry method [58].

4. Conclusions

In conclusion, the Fe-based R–P structure $Sr_3Fe_{2-x}Cu_xO_{7-\delta}$ oxides were prepared with the sol–gel method and evaluated as efficient cathodes for SOFCs. Among all the electrode materials, the SFC10 cathode provides satisfactory electrochemical activity for ORR with a low R_p value of 0.11 Ω cm^2 at 700 °C. The SFC10 cathode-based fuel cell delivers outstanding PPD of 955 mW cm^{-2} and durability for 60 h at 700 °C. The satisfactory electrochemical activity of the SFC10 electrode is mainly because of the improved electrical conductivity and oxygen surface exchange capability. These superior performances verify

that Cu-doping is an effective strategy to improve the electrochemical performance of the electrode, and SFC10 is a promising electrode electrocatalyst for SOFCs.

Supplementary Materials: The following are available online at https://www.mdpi.com/article/10.3390/catal11111400/s1, Figure S1: Bode plots of the SFC10 cathode under different oxygen partial pressures, Figure S2: The schematic of the anode-supported single cell, Figure S3: *I-V* and *I-P* curves of the single cells with SFC10 cathode at 600–700 °C, Table S1: Lattice parameters of the SFC*x* oxides.

Author Contributions: L.P. and Q.L. conceived and designed the experiments, and performed the experiments; L.S. contributed reagents/materials/analysis tools; H.Z. analyzed the data; L.P. and Q.L. wrote the paper. All authors have read and agreed to the published version of the manuscript.

Funding: The project was supported by National Natural Science Foundation of China (51972100) and Heilongjiang Provincial Fund for Distinguished Young Scholars (JC2018014).

Acknowledgments: We are grateful to our Department of Instrumental Analysis for the analysis of TEM.

Conflicts of Interest: The authors declare no conflict of interest.

References

1. Brett, D.J.L.; Atkinson, A.; Brandon, N.P.; Skinner, S.J. Intermediate temperature solid oxide fuel cells. *Chem. Soc. Rev.* **2008**, *37*, 1568–1578. [CrossRef]
2. Jacobs, R.; Mayeshiba, T.; Booske, J.; Morgan, D. Material discovery and design principles for stable, high activity perovskite cathodes for solid oxide fuel cells. *Adv. Energy Mater.* **2018**, *8*, 1702708. [CrossRef]
3. Xu, X.M.; Pan, Y.L.; Zhong, Y.J.; Ran, R.; Shao, Z.P. Ruddlesden–popper perovskites in electrocatalysis. *Mater. Horiz.* **2020**, *7*, 2519–2565. [CrossRef]
4. Beppu, K.; Hosokawa, S.; Teramura, K.; Tanaka, T. Oxygen storage capacity of $Sr_3Fe_2O_{7-\delta}$ having high structural stability. *J. Mater. Chem. A* **2015**, *3*, 13540–13545. [CrossRef]
5. Kagomiya, I.; Jimbo, K.; Kakimoto, K.; Nakayama, M.; Masson, O. Oxygen vacancy formation and the ion migration mechanism in layered perovskite $(Sr, La)_3Fe_2O_{7-\delta}$. *Phys. Chem. Chem. Phys.* **2014**, *16*, 10875–10882. [CrossRef] [PubMed]
6. Ding, P.P.; Li, W.L.; Zhao, H.W.; Wu, C.C.; Wang, S.M. Review on Ruddlesden-Popper perovskites as cathode for solid oxide fuel cells. *J. Phys. Mater.* **2021**, *4*, 22002. [CrossRef]
7. Li, P.Z.; Yang, W.; Tian, C.J.; Zhao, W.Y.; Lü, Z.; Xie, Z.P.; Wang, C.A. Electrochemical performance of $La_2NiO_{4+\delta}$–$Ce_{0.55}La_{0.45}O_{2-\delta}$ as a promising bifunctional oxygen electrode for reversible solid oxide cells. *J. Adv. Ceram.* **2021**, *1*, 328–337. [CrossRef]
8. Ferchaud, C.; Grenier, J.C.; Zhang-Steenwinkel, Y.; van Tuel, M.M.A.; van Berkel, F.P.F.; Bassat, J.M. High performance praseodymium nickelate oxide cathode for low temperature solid oxide fuel cell. *J. Power Source* **2011**, *196*, 1872–1879. [CrossRef]
9. Mazo, G.N.; Mamaev, Y.A.; Galin, M.Z.; Kaluzhskikh, M.S.; Ivanov-Schitz, A.K. Structural and transport properties of the layered cuprate Pr_2CuO_4. *Inorg. Mater.* **2011**, *47*, 1218–1226. [CrossRef]
10. Chen, X.; Wang, J.Q.; Liang, Q.W.; Sun, X.; Zhu, X.F.; Zhou, D.F.; Meng, J. Pr_2NiO_4-$Pr_{0.2}Ce_{0.8}O_{1.9}$ composite cathode as a potential cathode material for intermediate temperature solid oxide fuel cells. *Solid State Sci.* **2020**, *100*, 106–108. [CrossRef]
11. Sun, C.; Li, Q.; Sun, L.P.; Zhao, H.; Huo, L.H. Characterization and electrochemical performances of Pr_2CuO_4 as a cathode material for intermediate temperature solid oxide fuel cells. *Mater. Res. Bull.* **2014**, *53*, 65–69. [CrossRef]
12. Ling, Y.; Wang, F.; Budiman, R.A.; Nakamura, T.; Amezawa, K. Oxygen non-stoichiometry, the defect equilibrium model and thermodynamic quantities of the Ruddlesden-Popper oxide $Sr_3Fe_2O_{7-\delta}$. *Phys. Chem. Chem. Phys.* **2015**, *17*, 7489–7497. [CrossRef]
13. Ling, Y.; Wang, F.; Okamoto, Y.; Nakamura, T.; Amezawa, K. Oxygen non-stoichiometry and thermodynamic quantities in the Ruddlesden-Popper oxides $La_xSr_{3-x}Fe_2O_{7-\delta}$. *Solid State Ion.* **2016**, *288*, 298–302. [CrossRef]
14. Wang, Z.Q.; Yang, W.Q.; Shafi, S.P.; Bi, L.; Wang, Z.B.; Peng, R.R.; Xia, C.R.; Liu, W.; Lu, Y.L. A high performance cathode for proton conducting solid oxide fuel cells. *J. Mater. Chem. A* **2015**, *3*, 8405–8412. [CrossRef]
15. Gil, D.M.; Boulahya, K.; Santoyo, M.S.; Azcondo, M.T.; Amador, U. Superior performance as cathode material for intermediate-temperature solid oxide fuel cells of the Ruddlesden-Popper n = 2 member $Eu_2SrCo_{0.50}Fe_{1.50}O_{7-\delta}$ with low cobalt content. *Inorg. Chem.* **2021**, *60*, 3094–3105.
16. Huan, D.M.; Wang, Z.Q.; Wang, Z.B.; Peng, R.R.; Xia, C.R. High-performanced cathode with a two-layered R-P structure for intermediate temperature solid oxide fuel cells. *ACS Appl. Mater. Interfaces* **2016**, *8*, 4592–4599. [CrossRef]
17. Liu, P.; Luo, Z.F.; Kong, J.R.; Yang, X.F.; Liu, Q.C.; Xu, H. $Ba_{0.5}Sr_{0.5}Co_{0.8}Fe_{0.2}O_{3-\delta}$-based dual-gradient cathodes for solid oxide fuel cells. *Ceram. Int.* **2018**, *44*, 4516–4519. [CrossRef]
18. Zhou, W.; Ran, R.; Shao, Z.P. Progress in understanding and development of $Ba_{0.5}Sr_{0.5}Co_{0.8}Fe_{0.2}O_{3-\delta}$-based cathodes for intermediate-temperature solid-oxide fuel cells: A review. *J. Power Source* **2009**, *1*, 231–246. [CrossRef]
19. Gao, L.; Zhu, M.Z.; Li, Q.; Sun, L.P.; Zhao, H.; Grenier, J.C. Electrode properties of Cu-doped $Bi_{0.5}Sr_{0.5}FeO_{3-\delta}$ cobalt-free perovskite as cathode for intermediate-temperature solid oxide fuel cells. *J. Alloy. Compd.* **2017**, *700*, 29–36. [CrossRef]

20. Yin, J.W.; Yin, Y.M.; Lu, J.; Zhang, C.; Ming, N.Q.; Ma, Z.F. Structure and properties of novel cobalt-free oxides $Nd_xSr_{1-x}Fe_{0.8}Cu_{0.2}O_{3-\delta}$ ($0.3 \leq x \leq 0.7$) as cathodes of intermediate temperature solid oxide fuel cells. *J. Phys. Chem. C* **2014**, *118*, 13357–13368. [CrossRef]
21. Jin, F.; Xu, H.; Wen, L.; Yu, S.; He, T. Characterization and evaluation of double perovskites $LnBaCoFeO_{5+\delta}$ (Ln=Pr and Nd) as intermediate-temperature solid oxide fuel cell cathodes, *J. Power Sources.* **2013**, *243*, 10–18. [CrossRef]
22. Xia, W.W.; Li, Q.; Sun, L.P.; Huo, L.H.; Zhao, H. Electrochemical performance of Sn-doped $Bi_{0.5}Sr_{0.5}FeO_{3-\delta}$ perovskite as cathode electrocatalyst for solid oxide fuel cells. *J. Alloy. Compd.* **2020**, *835*, 155406. [CrossRef]
23. Gou, M.L.; Ren, R.Z.; Sun, W.; Xu, C.M.; Meng, X.G.; Wang, Z.H.; Qiao, J.S.; Sun, K.N. Nb-doped $Sr_2Fe_{1.5}Mo_{0.5}O_{6-\delta}$ electrode with enhanced stability and electrochemical performance for symmetrical solid oxide fuel cells. *Ceram. Int.* **2019**, *45*, 15696–15704. [CrossRef]
24. Xia, W.W.; Li, Q.; Sun, L.P.; Huo, L.H.; Zhao, H. Enhanced electrochemical performance and CO_2 tolerance of $Ba_{0.95}La_{0.05}Fe_{0.85}Cu_{0.15}O_{3-\delta}$ as Fe-based cathode electrocatalyst for solid oxide fuel cells. *J. Eur. Ceram. Soc.* **2020**, *40*, 1967–1974. [CrossRef]
25. Niu, B.B.; Jin, F.J.; Zhang, L.L.; Shen, P.S.; He, T.M. Performance of double perovskite symmetrical electrode materials $Sr_2TiFe_{1-x}Mo_xO_{6-\delta}$ (x = 0.1, 0.2) for solid oxide fuel cells. *Electrochim. Acta* **2018**, *263*, 217–227. [CrossRef]
26. Subramania, A.; Saradha, T.; Muzhumathi, S. Synthesis of nano-crystalline $(Ba_{0.5}Sr_{0.5})Co_{0.8}Fe_{0.2}O_{3-\delta}$ cathode material by a novel sol-gel thermolysis process for IT-SOFCs. *J. Power Source* **2007**, *165*, 728–732. [CrossRef]
27. Zhang, Y.; Knibbe, R.; Sunarso, J.; Zhong, Y.J.; Zhou, W.; Shao, Z.P.; Zhu, Z.H. Recent progress on advanced materials for solid oxide fuel cells operating below 500 °C. *Adv. Mater.* **2017**, *29*, 1700132. [CrossRef]
28. Sun, C.Z.; Kong, Y.; Shao, L.; Sun, K.N.; Zhang, N.Q. Probing oxygen vacancy effect on oxygen reduction reaction of the $NdBaCo_2O_{5+\delta}$ cathode for solid oxide fuel cells. *J. Power Source* **2020**, *459*, 228017. [CrossRef]
29. Zhang, W.; Zhang, L.; Guan, K.; Zhang, X.; Meng, J. Effective promotion of oxygen reduction activity by rare earth doping in simple perovskite cathodes for intermediate-temperature solid oxide fuel cells. *J. Power Source* **2020**, *446*, 227360. [CrossRef]
30. Gao, L.; Zhu, M.Z.; Xia, T.; Li, Q.; Li, T.S.; Zhao, H. Ni-doped $BaFeO_{3-\delta}$ perovskite oxide as highly active cathode electrocatalyst for intermediate-temperature solid oxide fuel cells. *Electrochim. Acta* **2018**, *289*, 428–436. [CrossRef]
31. Dong, F.F.; Chen, D.J.; Chen, Y.B.; Zhao, Q.; Shao, Z.P. La-doped $BaFeO_{3-\delta}$ perovskite as a cobalt-free oxygen reduction electrode for solid oxide fuel cells with oxygen-ion conducting electrolyte. *J. Mater. Chem.* **2010**, *22*, 15071–15079. [CrossRef]
32. Huan, D.M.; Zhang, L.; Zhu, K.; Li, X.Y.; Peng, R.R. Oxygen vacancy-engineered cobalt-free Ruddlesden-Popper cathode with excellent CO_2 tolerance for solid oxide fuel cells. *J. Power Source* **2021**, *497*, 229872. [CrossRef]
33. Wang, J.; Lam, K.Y.; Saccoccio, M.; Gao, Y.; Chen, D.J.; Ciucci, F. Ca and In co-doped $BaFeO_{3-\delta}$ as a cobalt-free cathode material for intermediate-temperature solid oxide fuel cells. *J. Power Source* **2016**, *324*, 224–232. [CrossRef]
34. Ren, R.Z.; Wang, Z.H.; Meng, X.G.; Xu, C.M.; Qiao, J.S.; Sun, W.; Sun, K.N. Boosting the electrochemical performance of Fe-based layered double perovskite cathodes by Zn^{2+} doping for solid oxide fuel cells. *ACS Appl. Mater. Interfaces* **2020**, *12*, 23959–23967. [CrossRef]
35. Yao, C.G.; Zhang, H.X.; Liu, X.J.; Meng, J.L.; Meng, J.; Meng, F.Z. A niobium and tungsten co-doped $SrFeO_{3-\delta}$ perovskite as cathode for intermediate temperature solid oxide fuel cells. *Ceram. Int.* **2019**, *45*, 7351–7358. [CrossRef]
36. Li, Q.; Xian, T.; Sun, L.P.; Zhao, H.; Huo, L.H. Electrochemical performance of novel cobalt-free perovskite $SrFe_{0.7}Cu_{0.3}O_{3-\delta}$ cathode for intermediate temperature solid oxide fuel cells. *Electrochim. Acta* **2014**, *150*, 151–156. [CrossRef]
37. Fu, L.; Zhou, J.; Yang, J.M.; Lian, Z.J.; Wang, J.K.; Cheng, Y.H.; Wu, K. Exsolution of Cu nanoparticles in $(LaSr)_{0.9}Fe_{0.9}Cu_{0.1}O_4$ Ruddlesden-Popper oxide as symmetrical electrode for solid oxide cells. *Appl. Surf. Sci.* **2020**, *511*, 145525. [CrossRef]
38. Boulahya, K.; Hassan, M.; Munoz Gil, D.; Romero, J.; Herrero, A.G.; Martin, S.G.; Amador, U. Exploring the physical properties of $Eu_2SrCo_{1.5}Mn_{0.5}O_7$, a new n = 2 member of the Ruddlesden-Popper series $(Eu,Sr)_{n+1}(Co,Mn)_nO_{3n+1}$. *J. Mater. Chem. A* **2015**, *3*, 22931–22939. [CrossRef]
39. Boulahya, K.; Muñoz, D.; Gómez-Herrero, A.; Azcondo, M.T.; Amador, U. $Eu_2SrCo_{1.5}Fe_{0.5}O_7$ a new promising Ruddlesden-Popper member as a cathode component for intermediate temperature solid oxide fuel cells. *J. Mater. Chem. A* **2019**, *7*, 5601–5611. [CrossRef]
40. Huan, D.M.; Zhang, L.; Zhang, S.W.; Shi, N.; Li, X.Y.; Zhu, K.; Xia, C.R.; Peng, R.R.; Lu, Y.L. Ruddlesden-Popper oxide $SrEu_2Fe_2O_7$ as a promising symmetrical electrode for pure CO_2 electrolysis. *J. Mater. Chem. A* **2021**, *9*, 2706–2713. [CrossRef]
41. Kim, J.H.; Manthiram, A. Characterization of $Sr_{2.7}Ln_{0.3}Fe_{1.4}Co_{0.6}O_7$ (Ln = La, Nd, Sm, Gd) intergrowth oxides as cathodes for solid oxide fuel cells. *Solid State Ion.* **2009**, *180*, 1478–1483. [CrossRef]
42. Lou, Z.L.; Peng, J.; Dai, N.N.; Qiao, J.S.; Yan, Y.M.; Wang, Z.H.; Wang, J.W.; Sun, K.N. High performance $La_3Ni_2O_7$ cathode prepared by a facile sol-gel method for intermediate temperature solid oxide fuel cells. *Electrochem. Commun.* **2012**, *22*, 97–100. [CrossRef]
43. Ling, Y.H.; Li, T.; Yang, Y.; Tian, Y.F.; Wang, X.X.; Chen, K.X.; Dong, D.H.; Chen, Y.; Amezawa, K. Oxygen vacancies-rich iron-based perovskite-like electrodes for symmetrical solid oxide fuel cells. *Ceram. Int.* **2021**, *47*, 12916–12925. [CrossRef]
44. Kim, Y.D.; Yang, J.Y.; Saqib, M.; Park, K.; Shin, J.; Jo, M.; Park, K.M.; Lim, H.T.; Song, S.J.; Park, J.Y. Cobalt-free perovskite $Ba_{1-x}Nd_xFeO_{3-\delta}$ air electrode materials for reversible solid oxide cells. *Ceram. Int.* **2021**, *47*, 7985–7993. [CrossRef]
45. Idrees, A.; Jiang, X.N.; Liu, G.; Luo, H.; Jia, G.Q.; Zhang, Q.Y.; Jiang, L.; Li, X.N.; Xu, B.M. Structures and properties of $LaFe_{0.8}Cu_{0.2}O_{3-\delta}$ and $BaFe_{0.8}Cu_{0.2}O_{3-\delta}$ as cobalt-free perovskite-type cathode materials for the oxygen reduction reaction. *ChemistryOpen* **2018**, *7*, 688–695. [CrossRef]

46. Jung, D.W.; Kwak, C.; Park, H.J.; Kim, J.S.; Ahn, S.J.; Yeon, D.H.; Seo, S.; Moon, K.S.; Lee, S.M. High-performance perovskite $Ba_{0.5}Sr_{0.5}Co_{0.8}Fe_{0.1}Zn_{0.1}O_{3-\delta}$–$La_{0.6}Sr_{0.4}Co_{0.2}Fe_{0.8}O_{3-\delta}$ composite cathode. *Scr. Mater.* **2016**, *113*, 59–62. [CrossRef]
47. Ortiz-Vitoriano, N.; Hauch, A.; De Larramendi, I.R.; Bernuy-López, C.; Knibbe, R.; Rojo, T. Electrochemical characterization of $La_{0.6}Ca_{0.4}Fe_{0.8}Ni_{0.2}O_3$ cathode on $Ce_{0.8}Gd_{0.2}O_{1.9}$ electrolyte for IT-SOF. *Int. J. Hydrog. Energy* **2014**, *39*, 6675–6679. [CrossRef]
48. Jiang, Y.N.; Yang, Y.; Xia, C.R.; Bouwmeester, H.J.M. $Sr_2Fe_{1.4}Mn_{0.1}Mo_{0.5}O_{6-\delta}$ perovskite cathode for highly efficient CO_2 electrolysis. *J. Mater. Chem. A* **2019**, *7*, 22939–22949. [CrossRef]
49. Escudero, M.J.; Aguadero, A.; Alonso, J.A. A kinetic study of oxygen reduction reaction on La_2NiO_4 cathodes by means of impedance spectroscopy. *J. Electroanal. Chem.* **2007**, *611*, 107–116. [CrossRef]
50. Guo, M.M.; Xia, T.; Li, Q.; Sun, L.P.; Zhao, H. Boosting the electrocatalytic performance of Fe-based perovskite cathode electrocatalyst for solid oxide fuel cells. *J. Eur. Ceram. Soc.* **2021**, *41*, 6531–6538. [CrossRef]
51. Guo, M.M.; Li, Q.; Gao, J.T.; Sun, L.P.; Huo, L.H.; Zhao, H. Highly electrocatalytic active and durable Fe-based perovskite oxygen reduction electrode for solid oxide fuel cells. *J. Alloy. Compd.* **2021**, *858*, 158265. [CrossRef]
52. Takeda, Y.; Kanno, R.; Noda, M.; Yamamoto, O. Cathodic polarization phenomena of perovskite oxide electrodes with stabilized zirconia. *J. Electrochem. Soc.* **1987**, *134*, A2656–A2661. [CrossRef]
53. De Souza, R.A.; Kilner, J.A. Oxygen transport in $La_{1-x}Sr_xMn_{1-y}Co_yO_{3\pm\delta}$ perovskites Part II. oxygen surface exchange. *Solid State Ion.* **1999**, *126*, 153–161. [CrossRef]
54. Kim, J.; Kim, G.D.; Moon, W.; Park, Y.I.; Lee, W.H.; Kobayashi, K.; Nagai, M.; Kim, C.E. Characterization of LSM-YSZ composite electrode by ac impedance spectroscopy. *Solid State Ion.* **2001**, *143*, 379–389. [CrossRef]
55. Zhao, C.; Zhang, T.; He, Y.; Qu, L.W.; Zhou, Q.J. Preparation and performance of $Sr_3Fe_{2-x}Ni_xO_{7-\delta}$ (x = 0, 0.1, 0.2, 0.3) cathode for intermediate-temperature solid oxide fuel cells. *Chin. J. Inorg. Chem.* **2019**, *35*, 1027–1033.
56. Zhao, Y.Q.; Zhang, K.; Wei, Z.L.; Li, Z.B.; Wang, Y.; Zhu, Z.W.; Liu, T. Performance and distribution of relaxation times analysis of Ruddlesden-Popper oxide $Sr_3Fe_{1.3}Co_{0.2}Mo_{0.5}O_{7-\delta}$ as a potential cathode for protonic solid oxide fuel cells. *Electrochim. Acta* **2020**, *352*, 136444. [CrossRef]
57. Gao, L.; Li, Q.; Sun, L.P.; Xia, T.; Huo, L.H.; Zhao, H.; Grenier, J.C. Antimony-doped $Bi_{0.5}Sr_{0.5}FeO_{3-\delta}$ as a novel Fe-based oxygen reduction electrocatalyst for solid oxide fuel cells below 600 °C. *J. Mater. Chem. A* **2018**, *6*, 15221–15229. [CrossRef]
58. Mauvya, F.; Lalanne, C.; Bassat, J.M.; Grenier, J.C.; Zhao, H.; Dordor, P.; Stevens, P. Oxygen reduction on porous $Ln_2NiO_{4+\delta}$ electrodes. *J. Eur. Ceram. Soc.* **2005**, *25*, 2669–2672. [CrossRef]